Chemical Science

ROYAL SOCIETY OF CHEMISTRY

EDGE ARTICLE

View Article Online
View Journal | View Issue

Cite this: *Chem. Sci.*, 2025, **16**, 13883

All publication charges for this article have been paid for by the Royal Society of Chemistry

Received 6th May 2025
Accepted 18th June 2025

DOI: 10.1039/d5sc03270a

rsc.li/chemical-science

Distinct oxygen reduction pathways for solar H_2O_2 production by regulating unsaturated bonds in covalent organic frameworks†

Jie-Yu Yue,*[a] Zi-Xian Pan,[a] Yan Guo,[a] Peng Yang *[a] and Bo Tang *[ab]

Photocatalytic H_2O_2 generation *via* the two-electron oxygen reduction reaction ($2e^-$ ORR) is a highly sustainable approach, capable of proceeding *via* either a one-step or two-step $2e^-$ ORR route. Nonetheless, precise regulation of the $2e^-$ ORR pathways still remains a formidable challenge. Herein, for the first time, we modulate the $2e^-$ ORR pathway through unsaturated bond control in covalent organic frameworks (COFs). We synthesize a pair of isostructural COFs distinguished only by their unsaturated bonds. The alkyne-containing TY-COF favors the two-step $2e^-$ ORR route, whereas the alkene-containing TE-COF follows the one-step $2e^-$ ORR route. Without any sacrificial agents in O_2, the TY-COF and TE-COF display impressive H_2O_2 production rates of 6455 and 4804 μmol g^{-1} h^{-1}, respectively. Further theoretical results reveal that the regulation of unsaturated bonds alters the electron–hole distribution along the COF skeletons, prompting the reorganization of the catalytic centers for ORR (the benzene ring in TY-COFs and the triazine in TE-COFs), which leads to divergent ORR pathways. Additionally, free-standing TY-COF and TE-COF membranes, fabricated *via* the interfacial polymerization method, are also able to drive H_2O_2 photosynthesis. The present work offers a new strategy and valuable inspiration for modulating $2e^-$ ORR pathways *via* strategic architectural engineering of COFs.

Introduction

H_2O_2 is a multifaceted and eco-friendly oxidant, known for its broad range of applications in various industries, including chemical synthesis, environmental remediation, and medical sterilization.[1–3] The application of photocatalytic techniques, powered by solar energy, enables the generation of H_2O_2 *via* the oxygen reduction reaction (ORR) and water oxidation reaction (WOR), establishing a sustainable and cost-efficient strategy.[4–6] This method not only reduces energy consumption but also allows for on-site H_2O_2 generation, eliminating transportation and storage issues associated with concentrated H_2O_2 solutions.

In contrast to the kinetically sluggish WOR route, photosynthetic H_2O_2 production *via* the two-electron ORR ($2e^-$ ORR) path presents a more promising and readily implementable alternative.[7–9] Depending on the electron transfer processes and intermediates involved, the $2e^-$ ORR mechanism for H_2O_2 production can be classified into two divergent routes: the direct one-step $2e^-$ ORR route ($O_2 + 2e^- + 2H^+ \rightarrow H_2O_2$) and the sequential two-step $2e^-$ ORR route ($O_2 + e^- \rightarrow O_2^{\bullet-}$; $O_2^{\bullet-} + e + 2H^+ \rightarrow H_2O_2$).[4,5] The key distinction between the one-step and two-step $2e^-$ ORR lies in the formation of the $O_2^{\bullet-}$ intermediate. In numerous practical scenarios, particularly in aqueous environments containing geochemical metals and dissolved organic matter, the $O_2^{\bullet-}$ intermediate is prone to disproportionation,[10] which consequently results in diminished H_2O_2 production efficiency. As such, optimizing the $2e^-$ ORR pathway is essential for enabling *in situ* H_2O_2 generation with high efficiency across diverse practical contexts, yet it remains a formidable challenge.[11]

In the realm of materials explored for photocatalytic H_2O_2 production, covalent organic frameworks (COFs) have attracted considerable interest since 2020.[12–17] COFs are characterized by their crystalline, porous architectures, which are formed from organic building units linked together by covalent bonds. Their highly ordered structures, tunable pore sizes, and versatile functionalities render them ideal candidates for photocatalytic applications.[18–20] Furthermore, the precise control over their molecular design facilitates the rational engineering of COFs with enhanced light absorption, efficient charge separation, and optimized catalytic sites. These distinctive features establish COFs as promising platforms for the efficient and selective

[a]*Key Laboratory of Molecular and Nano Probes, Ministry of Education, Collaborative Innovation Center of Functionalized Probes for Chemical Imaging in Universities of Shandong, College of Chemistry, Chemical Engineering and Materials Science, Shandong Normal University, Jinan, 250014, P. R. China. E-mail: yuejieyu@sdnu.edu.cn; yangpeng@sdnu.edu.cn*

[b]*Laoshan Laboratory, Qingdao, 266200, P. R. China. E-mail: tangb@sdnu.edu.cn*

† Electronic supplementary information (ESI) available: Materials, measurements, experimental details, and supplementary figures. See DOI: https://doi.org/10.1039/d5sc03270a

photogeneration of H_2O_2.[21–27] To date, the majority of reported COFs generate H_2O_2 *via* the two-step $2e^-$ ORR route,[28–34] while only a few studies have successfully regulated the $2e^-$ ORR route.[35–37] For instance, FS-COF with sulfone units on the backbone,[35] PyIm-COF featuring pyridyl-imine structures,[36] and *s*-heptazine-based HEP-TAPT-COF can drive H_2O_2 generation through the one-step $2e^-$ ORR pathway.[37] Notwithstanding these advances, the strategic modulation of $2e^-$ ORR pathways within COFs architectures remains a nascent domain, necessitating the exploration of innovative design paradigms and synthetic methodologies.

Unsaturated bonds constitute covalent connections that link two atoms *via* multiple bonds, including triple and double bonds with hybridized orbitals, such as sp-hybridized alkyne bonds (–C≡C–), sp^2-hybridized alkene bonds (–C=C–), and azo bonds (–N=N–), which profoundly modulate the electronic states of organic materials. While COFs incorporating –C=C– and –N=N– have exhibited distinguished electrocatalytic and photocatalytic ORR activities,[38,39] the comparative impact of –C≡C– and –C=C– on the photocatalytic $2e^-$ ORR pathways for H_2O_2 production remains unexplored.

Herein, for the first time, we modulate the $2e^-$ ORR pathways in COFs by manipulating unsaturated bonds (–C≡C– and –C=C–) on the skeleton. We synthesize two structurally similar COFs (named TY-COF and TE-COF), which differ only in the type of unsaturated bonds (–C≡C– or –C=C–, Fig. 1a). Experimental results exhibit that the TY-COF, with –C≡C–, prefers the two-step $2e^-$ ORR route, while the TE-COF, with –C=C–, undergoes the one-step $2e^-$ ORR pathway. Without sacrificial agents in O_2, the TY-COF and TE-COF produce H_2O_2 at rates of 6455 and 4804 μmol g^{-1} h^{-1}, respectively, comparable to high-performance COF-based photocatalysts. Furthermore, TY-COF and TE-COF membranes are built *via* interfacial polymerization, which can also produce H_2O_2 smoothly. Theoretical calculations reveal that the regulation of unsaturated bonds alters the electron–hole distribution along the COF skeletons, changing the ORR catalytic centers (the benzene ring in TY-COFs and the triazine in TE-COFs), which ultimately leads to divergent $2e^-$ ORR pathways. The present work underscores the critical role of regulating the charge carrier distribution in catalysts to modulate the $2e^-$ ORR pathways.

Results and discussion

To elucidate the influence of unsaturated bonds on the photocatalytic performance and mechanism for H_2O_2 generation, we designed a pair of COFs with –C≡C– and –C=C–, respectively. As illustrated in Fig. 1a, the TY-COF was fabricated *via* the condensation of 4,4′,4″-(benzene-1,3,5-triyltris(ethyne-2,1-diyl)) trianiline (BYA) with 4,4′,4″-(1,3,5-triazine-2,4,6-triyl) tribenzaldehyde (TTB). The alkyne-containing BYA linker introduced –C≡C– into the framework, creating a rigid and highly conjugated structure. In parallel, the TE-COF was constructed using 4,4′,4″–((1*E*,1′*E*,1″*E*)-benzene-1,3,5-triyltris(ethene-2,1-diyl))trianiline (BEA) in conjunction with the same TTB monomer, thereby integrating –C=C– as the pivotal unsaturated bonds.

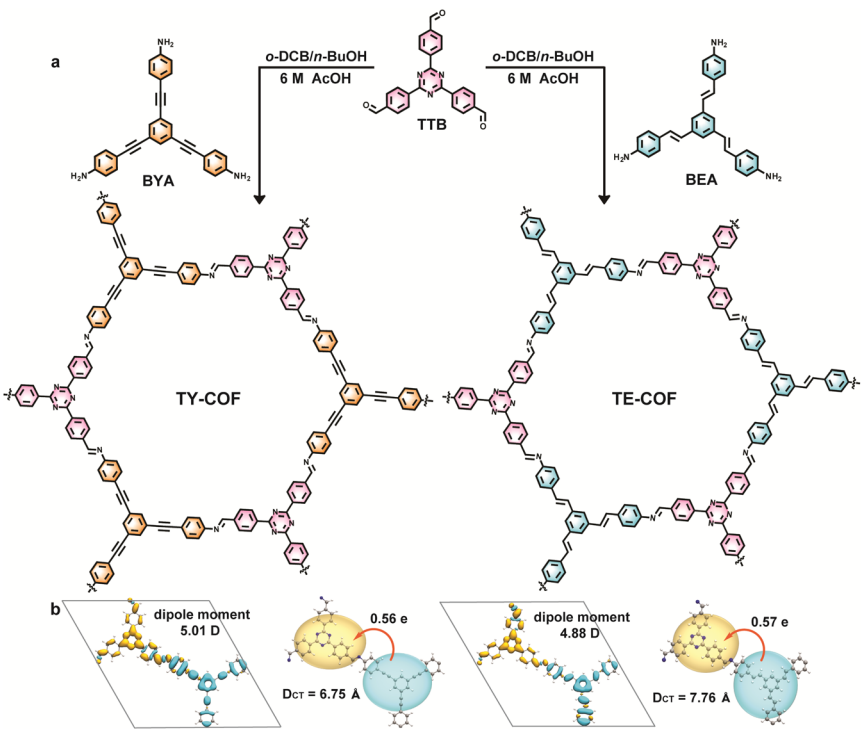

Fig. 1 (a) Chemical structures, (b) calculated electron–hole distributions, electron transfer amount, and electron transfer distances of TY-COFs and TE-COFs in the first excited state by TD-DFT calculations.

First of all, we investigated the electronic structure disparities between the TY-COF and TE-COF, emanating from the intrinsic nature of their unsaturated bonds through time-dependent density functional theory (TD-DFT) calculations using CP2K (2023.2). As shown in Fig. 1b, the TY-COF unit cell exhibited a pronounced dipole moment of 5.01 D, whereas the TE-COF unit cell showed a marginally diminished dipole moment of 4.88 D in their first excited state. Typically, enhanced dipole moments correlate with augmented charge separation driving forces.[40] To probe their photoinduced charge separation and transfer behaviors, we assessed the differences in charge density that existed between the ground state and the excited state for model compounds of both COFs. The centroid distributions of positive (blue regions) and negative charges (yellow regions) were distinctly localized in their respective segments. The electron transfer amounts (ΔE) of TY-COF and TE-COF were 0.56*e* and 0.57*e*, respectively, while the corresponding electron transfer distances (D_{CT}) of TY-COF and TE-COF were 6.75 Å and 7.76 Å. Generally, an elevated absolute value of $\Delta E/D_{CT}$ signifies more efficacious charge transfer.[41] Compared to the alkene-containing TE-COF, the alkyne-containing TY-COF demonstrated a more substantial dipole moment and pronounced charge transfer characteristics. These predicted subtle yet consequential distinctions suggest that the –C≡C– and –C=C– linkages could generate distinctive electronic environments within the COF architectures, potentially modulating charge transfer dynamics during photocatalytic processes.

To confirm the crystallinity of TY-COF and TE-COF, powder X-ray diffraction (PXRD) analysis was conducted. As shown in Fig. 2a, the TY-COF exhibited a pronounced diffraction peak at 3.50°, accompanied by two weaker peaks at 6.10° and 25.6°, corresponding to the (100), (110), and (001) reflection planes, respectively. The experimental PXRD pattern aligned well with the simulated pattern based on the AA stacking mode. The Pawley-refined cell parameters of TY-COF were $a = b = 29.92$ Å, $c = 3.48$ Å, $\alpha = \beta = 90°$, and $\gamma = 120°$ ($R_{wp} = 2.78\%$ and $R_p = 2.19\%$). The experimental PXRD profile of TE-COF (Fig. 2b) illustrated a prominent peak at 3.38° and weaker peaks at 5.90°, 6.86°, 9.10°, and around 25.5°, related to the (100), (110), (200), (210), and (001) planes, respectively. The positions of the experimental PXRD peaks for the TE-COF closely matched the simulated results obtained using the AA stacking mode. The lattice parameters of TE-COF were found to be $a = b = 29.99$ Å, $c = 3.47$ Å, $\alpha = \beta = 90°$, and $\gamma = 120°$ ($R_{wp} = 2.64\%$ and $R_p = 2.10\%$). The slight shift in the primary diffraction peak position between the TY-COF and TE-COF (3.50° *vs.* 3.38°) reflected the structural variations introduced by the –C≡C– and –C=C– modules.

The permanent porosities of TY-COF and TE-COF were assessed *via* N_2 adsorption–desorption isotherms at 77 K. As depicted in Fig. 2c, the TY-COF featured a type IV isotherm, and the Brunauer–Emmett–Teller (BET) surface area was 350.3 $m^2 g^{-1}$. The pore size distribution analysis (inset of Fig. 2c) revealed a predominant pore width of approximately 2.41 nm for the TY-COF. In contrast, the TE-COF displayed a lower N_2 uptake capacity (Fig. 2d), resulting in a BET surface area of 174.8 $m^2 g^{-1}$. This reduced surface area, compared to the TY-COF, can be attributed to the distinct geometric configurations of the alkene linkages, which may introduce slight distortions within the

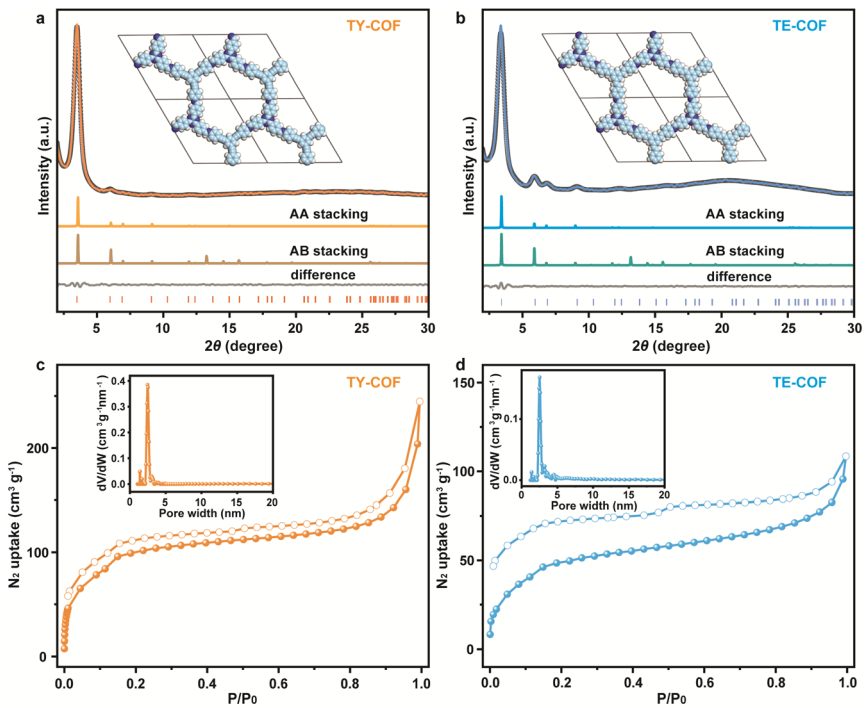

Fig. 2 Experimental, Pawley refined, and simulated PXRD patterns of (a) TY-COF and (b) TE-COF. N_2 sorption isotherms (insets: pore size distribution curves) of (c) TY-COF and (d) TE-COF.

frameworks. Nevertheless, the TE-COF maintained a type IV isotherm with a pore size distribution centered around 2.53 nm (inset of Fig. 2d).

Fourier transform infrared (FT-IR) spectroscopy data were recorded to characterize the chemical structures of TY-COF and TE-COF. Fig. S1† presents the comparative FT-IR spectra of the monomers (BEA, BYA, and TTB) and the resultant COFs (TY-COF and TE-COF), offering crucial insights into their molecular structures and bonding characteristics. The FT-IR spectra of both the TY-COF and TE-COF displayed distinctive –C═N stretching vibration bands, serving as definitive evidence for the formation of imine linkages during the condensation reactions. Specifically, the TY-COF exhibited a characteristic –C═N stretching band at 1622 cm^{-1}, while the TE-COF showed a similar but slightly shifted band at 1616 cm^{-1}. Solid-state ^{13}C nuclear magnetic resonance (NMR) spectroscopy was carried out on both TY-COF and TE-COF to further validate the successful formation of the intended COFs (Fig. S2†). Signals at 154.9 and 156.3 ppm were attributed to the carbon atoms in the C═N bonds of TY-COF and TE-COF, respectively. Signals at 169.7 and 169.5 ppm were identified as the carbon atoms within the triazine unit of TY-COF and TE-COF, respectively. Additionally, the peak at 89.8 ppm was characteristic of carbon atoms in the –C≡C– linkage, providing direct evidence for the incorporation of the alkyne-containing building blocks into the TY-COF structure. The establishment of TY-COF and TE-COF was further substantiated by X-ray photoelectron spectroscopy (XPS) measurements illustrated in Fig. S3,† along with elemental analysis results provided in Table S1.†

Thermogravimetric analysis (TGA) was utilized to evaluate the thermal robustness of the TY-COF and TE-COF (Fig. S4†). The as-synthesized COFs exhibited a weight loss of less than 5% at 400 °C, which signified their commendable thermal stability. The solvent stability of the TY-COF and TE-COF was assessed through PXRD analysis after treating them in various solvents and under different pH conditions for 8 h. Both TY-COF and TE-COF retained their crystallinity under these conditions, underscoring their potential applicability in diverse settings (Fig. S5†).

To obtain a more comprehensive understanding of the morphological features and nanostructure of TE-COF and TY-COF, both scanning electron microscopy (SEM) and transmission electron microscopy (TEM) analyses were conducted. The TY-COF exhibited an adherent particle stacking morphology (Fig. S6a†). The TE-COF displayed granular structures and coral-like structures in Fig. S6b.† The morphologies of TY-COF and TE-COF observed by TEM (Fig. S6c and d†) were consistent with their SEM images. Besides, we carried out high-resolution transmission electron microscopy (HRTEM) to check the lattice structures of TY-COF and TE-COF. Notably, while lattice fringes were not discernible in the TY-COF, the TE-COF revealed pronounced lattice fringes attributable to the (001) plane (Fig. S6e†).

Afterwards, the optical and electronic properties of TY-COF and TE-COF were investigated. As illustrated in the UV-visible diffuse reflectance spectra (UV-vis DRS) in Fig. 3a, the TY-COF exhibited broad absorption ranges with an edge extending to approximately 480 nm, whereas the TE-COF displayed a slightly red-shifted absorption edge around 540 nm. The corresponding Tauc plots (inset, Fig. 3a) yielded optical bandgaps of 2.54 eV for the TY-COF and 2.29 eV for the TE-COF. The Mott–Schottky plots of TY-COF and TE-COF (Fig. S7†) revealed positive slopes, indicating their n-type semiconductor characteristics, with flat band potentials of −0.99 and −0.89 V (*vs.* Ag/AgCl). Based on these optical bandgaps and flat band potentials, we constructed the energy band diagrams for TY-COF and TE-COF (Fig. 3b). The

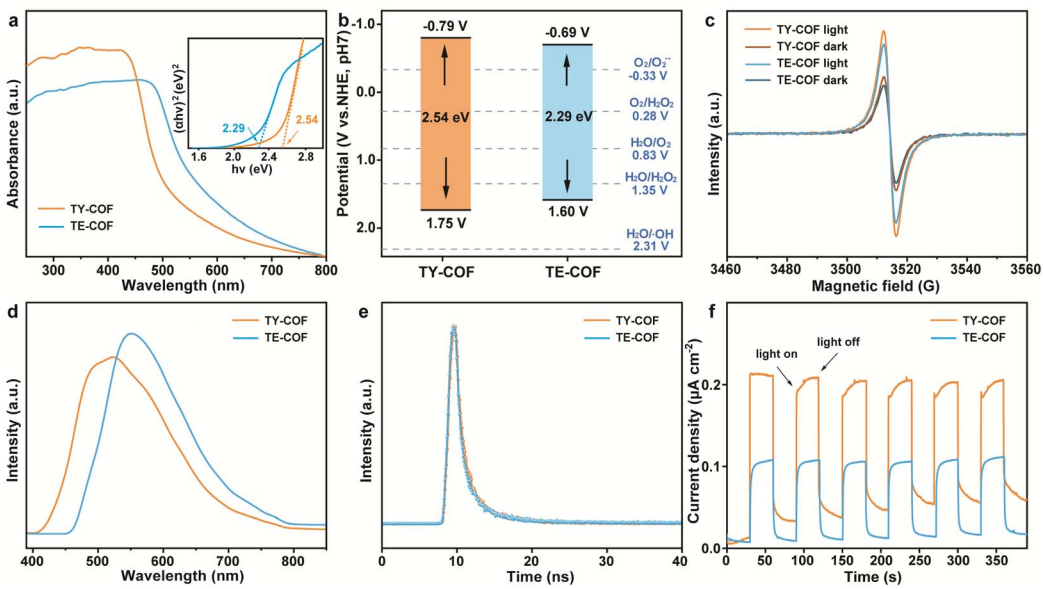

Fig. 3 (a) UV-vis DRS with Tauc plots, (b) energy band structures, (c) EPR spectra (under dark and light irradiation), (d) PL spectra, (e) time-resolved PL decay curves (excited at 375 nm), and (f) transient photocurrent density of the TY-COF and TE-COF.

TY-COF exhibited a conduction band (CB) potential of −0.79 V (*vs.* NHE) and a valence band (VB) potential of 1.75 V (*vs.* NHE). In contrast, the TE-COF exhibited CB potentials of −0.69 V (*vs.* NHE) and VB potentials of 1.60 V (*vs.* NHE). Obviously, both TY-COF and TE-COF are thermodynamically favorable for photocatalytic H_2O_2 production *via* ORR and WOR pathways.

To directly observe the unpaired electrons in TY-COF and TE-COF, we conducted electron paramagnetic resonance (EPR) spectroscopy under both dark and illuminated conditions (Fig. 3c). Both COFs showed *g* values close to 2.003, with significantly enhanced signal intensities under illumination compared to dark conditions. The TY-COF displayed a more obvious EPR signal than the TE-COF, indicating a superior capacity for generating photoinduced electrons at its CB, under light irradiation, compared to TE-COF, beneficial to the photocatalytic reaction.

Steady-state photoluminescence (PL) spectra (Fig. 3d) revealed distinct emission profiles for the as-synthesized COFs. The TY-COF showed an emission maximum at approximately 515 nm, while the TE-COF exhibited a red-shifted emission peak centered at 550 nm. The variation in emission wavelengths reflected their distinctive excited-state energy landscapes, influenced by the nature of their unsaturated bonds. Notably, the TY-COF displayed lower PL intensity compared to the TE-COF, indicating reduced radiative recombination of photogenerated charge carriers. This observation implied that the –C≡C– linkage in TY-COF facilitated more efficient charge separation and transfer, potentially enhancing its photocatalytic performance.

Time-resolved photoluminescence decay measurements (Fig. 3e) provided further insights into charge carrier dynamics. Both TY-COF and TE-COF displayed similar bi-exponential decay profiles, with average fluorescence lifetimes of 2.80 and 2.71 ns, respectively. The slightly longer lifetime observed in the TY-COF may contribute to enhanced charge separation efficiency, allowing photogenerated electrons additional time to engage in catalytic reactions prior to recombination.

Moreover, under intermittent illumination, the TY-COF generated a substantially higher photocurrent density than the TE-COF (Fig. 3f). This nearly two-fold enhancement in photocurrent for the TY-COF indicated superior charge separation and transport properties, consistent with the findings from EPR and PL analyses. Besides, electrochemical impedance spectroscopy (EIS) was applied to elucidate the charge transfer properties and electrical conductivity of TY-COF and TE-COF (Fig. S8†). The smaller radius in the Nyquist plots of the TY-COF indicated a substantially lower charge transfer resistance compared to the TE-COF. All the above characterization studies proved that the TY-COF featured more efficient charge transfer capabilities than the TE-COF, in accordance with the theoretically predicted results shown in Fig. 1.

Next, we systematically investigated the photocatalytic H_2O_2 generation performance of the TY-COF and TE-COF to elucidate how their distinct unsaturated bonds influence the reaction pathways and efficiency. All H_2O_2 concentrations were quantified using the titanium sulphate colorimetric method (Fig. S9†). The time-dependent H_2O_2 production of TY-COF and TE-COF under visible light irradiation (λ > 420 nm) in air and pure water is depicted in Fig. 4a, and TY-COF and TE-COF displayed H_2O_2 photogeneration rates of 5772 and 4429 μmol g^{-1} h^{-1}. The superior performance of the TY-COF aligned with its enhanced charge separation and transfer capabilities.

Furthermore, the kinetic parameters governing H_2O_2 production, specifically the formation (k_f) and decomposition (k_d) rate constants, were systematically determined for both TY-COF and TE-COF (Fig. S10†).[31] The k_f values for TY-COF and TE-COF were ascertained to be 0.84 and 0.77 mM h^{-1}, respectively, while their corresponding k_d values were 0.52 and 0.49 h^{-1}, respectively. Throughout the 12 h photocatalytic process, the H_2O_2 photosynthetic activity of the TY-COF consistently outperformed that of the TE-COF (Fig. S11†). Furthermore, the H_2O_2 production rates of TY-COF and TE-COF did not decrease significantly over five consecutive photocatalytic cycles (Fig. S12†). After 12 h of photocatalytic H_2O_2 experiments and 5 photocatalytic cycles, both TY-COF and TE-COF maintained their crystallinity and chemical structures, as confirmed by the PXRD curves (Fig. S13†), FT-IR spectra (Fig. S14†), and XPS spectra (Fig. S15†).

To elucidate the reaction pathways involved in H_2O_2 generation, we conducted experiments under varying atmospheric conditions (Fig. 4b). Both TY-COF and TE-COF exhibited the highest H_2O_2 production rates in a pure O_2 atmosphere (6455 μmol g^{-1} h^{-1} for the TY-COF, and 4804 μmol g^{-1} h^{-1} for the TE-COF), with solar-to-chemical conversion (SCC) efficiencies of 0.67% and 0.45%, respectively, among the highest reported for COF-based photocatalysts for H_2O_2 production (Tab. S2). The apparent quantum efficiencies (AQE) of TY-COF and TE-COF were measured at different wavelengths (420, 450, and 520 nm), respectively. As illustrated in Fig. S16,† both TY-COF and TE-COF exhibited the highest AQE at 450 nm (9.5% for TY-COF, 6.0% for TE-COF). Since TY-COF and TE-COF can drive H_2O_2 synthesis *via* the $2e^-$ ORR and $2e^-$ WOR pathways, the turnover number (TON) was calculated by dividing the amount of H_2O_2 generated by the amount of photocatalyst.[23,42] In O_2 and pure water, the TON values of TY-COF and TE-COF for H_2O_2 photogeneration were determined to be 4.92 and 3.69, respectively.

Besides, with the addition of sacrificial agents, such as EtOH and BnOH (10%), the H_2O_2 photogeneration rates of TY-COF (8121 and 39 060 μmol g^{-1} h^{-1}) and TE-COF (6023 and 34 351 μmol g^{-1} h^{-1}) were all enhanced (Fig. S17†). Exceptionally, TY-COF and TE-COF still showed measurable H_2O_2 production even in an Ar atmosphere, albeit at significantly reduced rates (370 μmol g^{-1} h^{-1} for TY-COF, and 44 μmol g^{-1} h^{-1} for TE-COF). This observation showed that TY-COF and TE-COF can photosynthesize H_2O_2 *via* the ORR and WOR dual pathways, with the ORR path playing a predominant role.[43] The TY-COF and TE-COF showed weak H_2O_2 decomposition efficiency in Ar (Fig. S18†).

To further explore the H_2O_2 photogeneration mechanisms *via* the $2e^-$ ORR channel in TY-COF and TE-COF, we conducted scavenger experiments utilizing 4-hydroxy-2,2,6,6-tetramethylpiperidine-*N*-oxyl (TEMPOL, for $O_2^{\bullet-}$), benzoquinone (BQ for $O_2^{\bullet-}$), and $KBrO_3$ (for electrons) in Fig. 4c. The introduction of $KBrO_3$ resulted in a significant decrease in H_2O_2 production

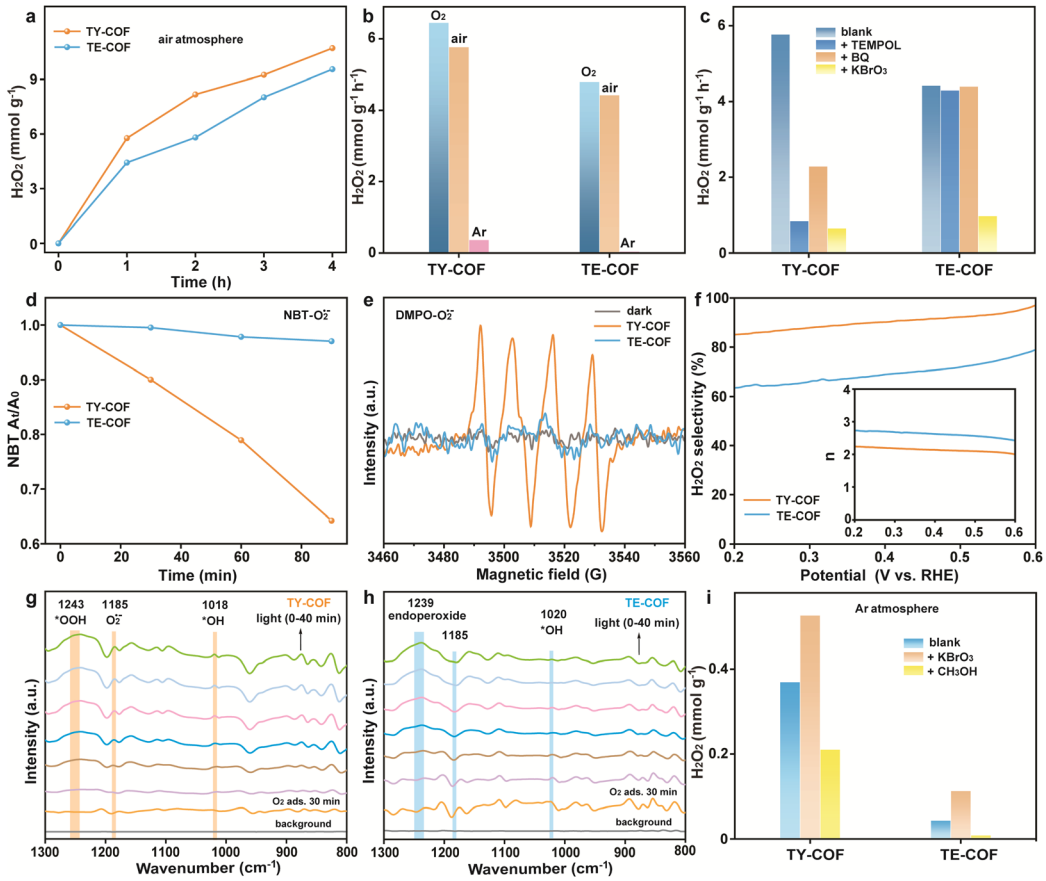

Fig. 4 (a) Time-dependent H_2O_2 photogeneration amount over TY-COF and TE-COF in air and pure water under visible light irradiation ($\lambda >$ 420 nm, Xe lamp). (b) The H_2O_2 photogeneration rate of TY-COF and TE-COF in O_2, air, and Ar atmospheres, respectively. (c) H_2O_2 yields of TY-COF and TE-COF in the presence of TEMPOL (1 mM), BQ (0.01 mM), and $KBrO_3$ (1 mM) in air and pure water under illumination for 1 h, respectively. (d) Detection of $O_2^{\bullet-}$ using NBT in TY-COF and TE-COF photocatalytic systems. (e) DMPO spin-trapping signals of $O_2^{\bullet-}$ of TY-COF and TE-COF. (f) H_2O_2 selectivity and electron transfer numbers of TY-COF and TE-COF tested by RRDE (KOH, 0.1 M). *In situ* DRIFT spectra of (g) TY-COF and (h) TE-COF during the H_2O_2 photoproduction process. (i) Quantity of H_2O_2 generated over TY-COF and TE-COF in Ar when $KBrO_3$ (1 mM) and CH_3OH (10%) were present.

for both TY-COF and TE-COF, suggesting that electrons played a crucial role in their H_2O_2 synthesis processes. For the TY-COF, the addition of TEMPOL and BQ dramatically suppressed H_2O_2 production, whereas the TE-COF exhibited minimal changes in H_2O_2 amount upon the addition of these scavengers. These distinct results confirmed that $O_2^{\bullet-}$ is a critical intermediate in the $2e^-$ ORR path of TY-COF, while it has a negligible impact on the H_2O_2 generation rate of TE-COF. Furthermore, the formation of $O_2^{\bullet-}$ during the photocatalytic processes of TY-COF and TE-COF was investigated using nitro blue tetrazolium (NBT) as a probe (Fig. 4d). The TY-COF exhibited a significant and continuous decrease in the absorbance intensity ratio (A_t/A_0) at a wavelength of 259 nm over time, reaching approximately 64% after 90 min, indicating substantial $O_2^{\bullet-}$ generation, whereas that of TE-COF showed almost no changes, suggesting minimal $O_2^{\bullet-}$ production. These findings were further corroborated by EPR spectra using 5,5-dimethyl-1-pyrroline *N*-oxide (DMPO) as a spin-trapping agent for $O_2^{\bullet-}$ (Fig. 4e). Under light irradiation, the TY-COF produced strong characteristic signals of the DMPO-$O_2^{\bullet-}$ adduct, while the TE-COF showed only weak signals, confirming the significantly higher $O_2^{\bullet-}$ generation capacity of the TY-COF. Together with the $O_2^{\bullet-}$ scavenger experiments, the NBT and EPR characterization of $O_2^{\bullet-}$ in the TY-COF and TE-COF photocatalytic systems, it can be deduced that TY-COF and TE-COF underwent divergent $2e^-$ ORR pathways. The TY-COF followed the two-step $2e^-$ ORR pathway, while the TE-COF adopted the one-step $2e^-$ ORR pathway for H_2O_2 photoproduction. By modulating the unsaturated bonds (–C≡C– and –C=C–) in the TY-COF and TE-COF, the $2e^-$ ORR pathways can be effectively regulated.

Additionally, the H_2O_2 selectivity and electron transfer numbers during the ORR of TY-COF and TE-COF were quantitatively assessed by rotating ring-disk electrode (RRDE) measurements (Fig. 4f). The TY-COF exhibited high H_2O_2 selectivity (85–98%) across the potential range of 0.2–0.6 V (*vs.* RHE), with electron transfer numbers approaching 2, indicating a predominant $2e^-$ ORR pathway. The TE-COF showed H_2O_2 selectivity of 65–78% with electron transfer numbers close to 2.6. These electrochemical results further supported the conclusion that the TY-COF and TE-COF mainly adopted $2e^-$ ORR pathways for H_2O_2 production.

To gain deeper insights into the reaction intermediates and pathways during the photocatalytic H_2O_2 evolution processes of TY-COF and TE-COF, *in situ* diffuse reflectance FT-IR (DRIFT) spectra were collected. For TY-COF (Fig. 4g), characteristic peaks at 1018 cm^{-1} (*OH), 1185 cm^{-1} ($O_2^{\bullet-}$), and 1243 cm^{-1} (*OOH) were observed during light irradiation, with signal intensities increasing over time. These spectral features indicated that the TY-COF predominantly followed a sequential O_2–$O_2^{\bullet-}$–*OOH–H_2O_2 pathway, consistent with its two-step $2e^-$ ORR mechanism. In contrast, the TE-COF (Fig. 4h) showed a strong peak at 1020 cm^{-1} (*OH) and 1239 cm^{-1} (endoperoxide),[35,36] The absence of $O_2^{\bullet-}$ signals suggested that the TE-COF operated through a different mechanism involving the formation of endoperoxide between O_2 and the TE-COF backbone *via* the one-step $2e^-$ ORR path.

To further distinguish the WOR pathways ($2e^-$ WOR or $4e^-$ WOR) of the as-synthesized COFs, we conducted control experiments in an Ar atmosphere with the addition of $KBrO_3$ and CH_3OH (a hole scavenger), as shown in Fig. 4i, respectively. In both TY-COF and TE-COF reaction systems, $KBrO_3$ significantly enhanced H_2O_2 production, while CH_3OH suppressed it. Moreover, even with the addition of $AgNO_3$, no O_2 could be detected by online gas chromatography (5A molecular sieve column), as shown in Fig. S19.† Combined with the scavenger experiments in Ar and the VB position, it can be concluded that both TY-COF and TE-COF underwent the direct $2e^-$ WOR pathway.

Based on the charge distribution observed in the first excited state of TY-COF and TE-COF illustrated in Fig. 1b, it was evident that the photoinduced electrons were predominantly localized within the units derived from the amine precursors, while the holes were primarily associated with the modules originating from the aldehyde monomers. To gain a more profound mechanistic understanding of the photocatalytic H_2O_2 generation processes in TY-COF and TE-COF, we further performed theoretical calculations to analyze the charge distribution on the representative fragments of the TY-COF and TE-COF using the transition density matrix (TDM) method.[44,45] As illustrated in Fig. 5a and b, the TDM heat maps unveiled distinct charge distribution patterns within TY-COF and TE-COF. In TY-COF (Fig. 5a), photogenerated holes predominantly accumulated at fragment 4 (34.2%), corresponding to the phenyl ring. Meanwhile, electrons were primarily localized at fragment 2 (43.3%), associated with the phenyl ring adjacent to the triazine unit.

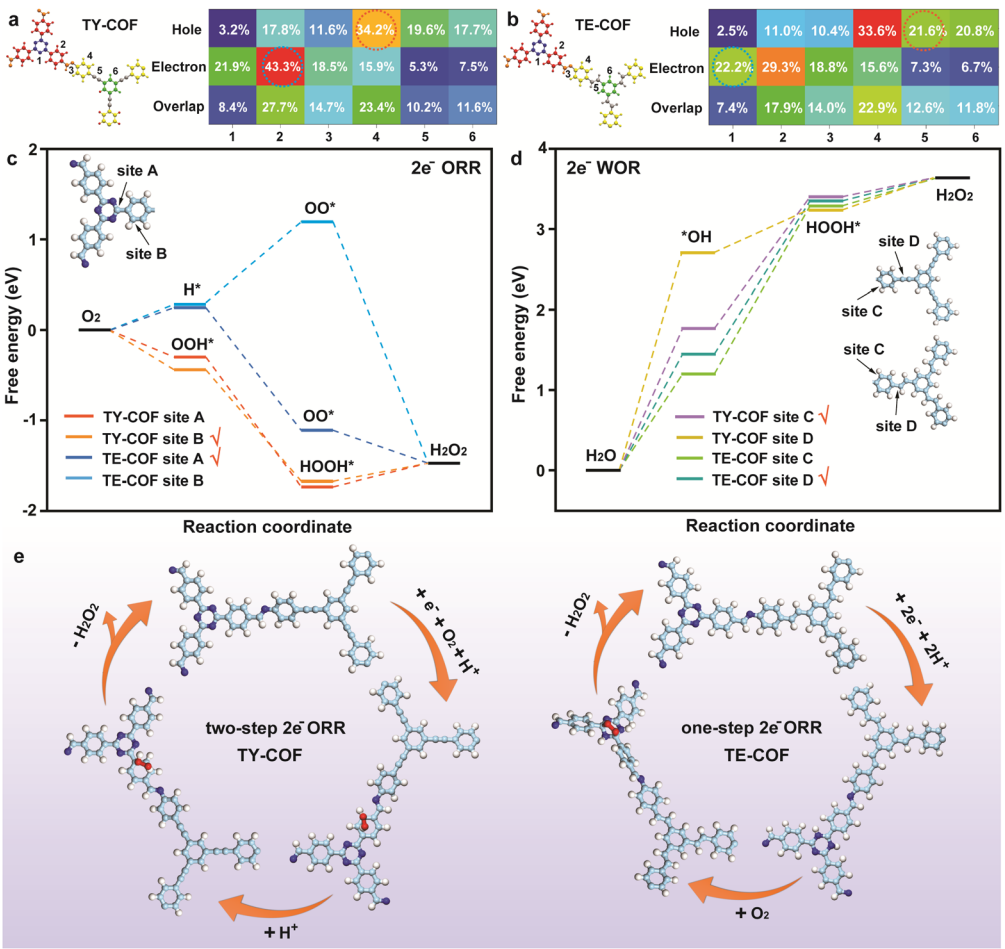

Fig. 5 Fragments chosen for TDM analysis and the heat map of hole–electron distributions of (a) TY-COF and (b) TE-COF. Free energy diagrams of photocatalytic H_2O_2 generation over TY-COF and TE-COF *via* (c) $2e^-$ ORR paths and (d) $2e^-$ WOR paths. (e) Proposed $2e^-$ ORR mechanism for H_2O_2 photoproduction *via* TY-COF and TE-COF.

Conversely, the TE-COF (Fig. 5b) displayed hole distribution at fragment 4 (phenyl ring, 33.6%) and fragment 5 (alkene bond, 21.6%). The electron distribution in TE-COF was more dispersed between fragment 1 (triazine, 22.2%) and fragment 2 (phenyl ring, 29.3%), resulting in less pronounced electron–hole separation compared to TY-COF.

According to the TDM analysis, the identification of the probable active sites for the 2e$^-$ ORR was achieved by evaluating the O_2 adsorption energies in fragment 1 and fragment 2 (Fig. S20†) of TY-COF and TE-COF, while those for the 2e$^-$ WOR were acquired by evaluating the H_2O adsorption energies in fragment 4 and fragment 5 (Fig. S21†). After that, site A and site B were chosen to calculate the free energy diagrams for the 2e$^-$ ORR of TY-COF and TE-COF. Site C and site D were chosen to calculate the free energy diagrams for the 2e$^-$ WOR of TY-COF and TE-COF. As depicted in Fig. 5c, at site A and site B of the TY-COF, the formation of the OOH* intermediate was exergonic (−0.30 eV and −0.44 eV), and the subsequent conversion to HOOH* (−1.74 eV and −1.62 eV) was also thermodynamically favorable. During the two-step 2e$^-$ ORR of TY-COF, the desorption of H_2O_2 was the rate determining step (RDS), with energy barriers of 0.27 eV at site A and 0.15 eV at site B. Consequently, for TY-COF, the ORR active center was identified as site B (the carbon atom in the phenyl ring in fragment 2). Since the TE-COF followed the one-step 2e$^-$ ORR pathway, H* and OO* intermediates were involved.[11,37] For the TE-COF, in contrast to site B, site A (the carbon atom in the triazine unit) with lower energy barriers (0.25 eV) in the RDS (the formation of *H) was the most likely ORR active center. The modulation of unsaturated bonds resulted in differing electron distributions between TY-COF and TE-COF, ultimately altering the ORR active centers.

Regarding the 2e$^-$ WOR pathway (Fig. 5d), both COFs showed considerable uphill energy profiles, with the formation of *OH and *HOOH intermediates. For TY-COF, the generation of *OH constituted the RDS, exhibiting an activation energy barrier of 1.76 eV at site C, markedly lower than the corresponding barrier observed at site D (2.70 eV). Conversely, for TE-COF, the formation of *HOOH represented the RDS, exhibiting an energy barrier of 1.89 eV at site D, substantially reduced compared to the analogous barrier encountered at site C (2.13 eV). Apparently, based on the energy barriers, site C (the carbon atom in the phenyl ring) in the TY-COF and site D (the carbon atom in the alkene) in the TE-COF represented the most active sites for their 2e$^-$ WOR pathways. This thermodynamic limitation explained the limited H_2O_2 production observed under Ar, in accordance with our experimental results.

These theoretical insights corroborated our experimental findings, confirming that the 2e$^-$ ORR pathway was the dominant contributor to H_2O_2 production in both COFs, with TY-COF exhibiting superior performance due to its more efficient charge separation, heightened electron density at the active center, and more favorable reaction energetics. Intriguingly, the distinct electronic structures arising from the differing unsaturated bonds (–C≡C– in TY-COF and –C=C– in TE-COF) fundamentally transformed the catalytic centers, resulting in divergent 2e$^-$ ORR pathways, as depicted in Fig. 5e. In addition,

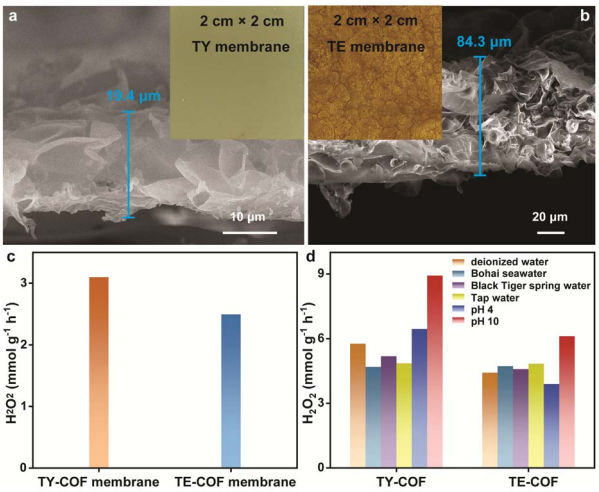

Fig. 6 Optical photographs and cross-sectional SEM images of the (a) TY-COF membrane and (b) TE-COF membrane. (c) H_2O_2 generation rates of the TY-COF membrane and TE-COF membrane in air and pure water. (d) H_2O_2 photoproduction rates of TY-COF and TE-COF in different waters.

the 2e$^-$ WOR mechanism for H_2O_2 photoproduction by TY-COF and TE-COF is illustrated in Fig. S22.†

In practical applications of H_2O_2 photogeneration, it is crucial and convenient that H_2O_2 can be easily separated. To this end, we fabricated free-standing TY-COF and TE-COF membranes *via* the interfacial polymerization method,[46,47] The PXRD patterns and FT-IR spectra shown in Fig. S23† confirmed the crystallinity and chemical structures of the TY-COF and TE-COF membranes. Both TY-COF and TE-COF membranes displayed surface morphologies with occasional bumps (Fig. S24†). The optical photographs and cross-sectional SEM images of TY-COF and TE-COF membranes are exhibited in Fig. 6a and b. Under air and pure water conditions, the TY-COF membrane (thickness: 19.4 μm) and the TE-COF membrane (thickness: 84.3 μm) can produce H_2O_2 smoothly at rates of 3100 and 2503 μmol g^{-1} h^{-1}, respectively (Fig. 6c).

Moreover, to ascertain the practical viability of solar-driven H_2O_2 production utilizing TY-COF and TE-COF, photocatalytic experiments were conducted across diverse aqueous matrices, including natural seawater, spring water, municipal tap water, acidic solution, and alkaline solution. As illustrated in Fig. 6d, both TY-COF and TE-COF demonstrated robust H_2O_2 generation capabilities across various aqueous environments, emphasizing their potential applicability in real world water treatment scenarios.

Conclusions

In conclusion, by rationally designing –C≡C– and –C=C– linkages into the skeletons of COFs, we successfully modulated the 2e$^-$ ORR pathways. Scavenger experiments, NBT probing, EPR spectra, and *in situ* DRIFT spectra confirmed that the –C≡C– incorporated TY-COF favored the two-step 2e$^-$ ORR pathway, while the –C=C– incorporated TE-COF followed the

one-step $2e^-$ ORR pathway. In the absence of sacrificial agents, the H_2O_2 evolution rates of TY-COF and TE-COF (6455 and 4804 μmol g^{-1} h^{-1}, respectively) were equivalent to those of high-performance COF-based photocatalysts. The SCC efficiencies of TY-COF and TE-COF were 0.67% and 0.45%, respectively. The outcomes of theoretical calculations suggested that the manipulation of unsaturated bonds induced a shift in the distribution of electrons and holes along the COF skeletons. This alteration led to a modification of the $2e^-$ ORR catalytic centers (the benzene ring in the TY-COF and triazine in the TE-COF), ultimately resulting in the emergence of two distinct $2e^-$ ORR pathways in TY-COF and TE-COF. Additionally, TY-COF and TE-COF membranes were constructed through an interfacial polymerization strategy, which can drive the H_2O_2 photosynthesis smoothly. This work highlights the critical role of manipulating charge carrier distribution in catalysts through structural design to modulate $2e^-$ ORR pathways.

Data availability

All the data supporting this article have been included in the main text and the ESI.†

Author contributions

J. Y. Y. designed the research, and wrote and revised the manuscript; Z. X. P. and Y. G. performed the experiments; P. Y. and B. T. provided financial support.

Conflicts of interest

The authors declare no competing financial interest.

Acknowledgements

This work was supported by the National Natural Science Foundation of China (22134004, 21804081, and 22278249), the Natural Science Foundation of Shandong Province (ZR2023MB063 and ZR2021YQ13), the Taishan Scholars Program of Shandong Province (tsqn202306151), and the Project of Shandong Provincial Center for Fundamental Science Research (YDZX2024150). The authors thank Suzhou Deyo Bot Advanced Materials Co., Ltd (**https://www.dy-test.com**) for support with material characterization.

Notes and references

1 Z. Chen, D. Yao, C. Chu and S. Mao, *Chem. Eng. J.*, 2023, **451**, 138489.
2 R. Liu, M. Zhang, F. Zhang, B. Zeng, X. Li, Z. Guo and X. Lang, *Small*, 2025, **21**, 2411625.
3 J.-Y. Yue, L.-P. Song, Y.-F. Fan, Z.-X. Pan, P. Yang, Y. Ma, Q. Xu and B. Tang, *Angew. Chem., Int. Ed.*, 2023, **62**, e202309624.
4 X. Zeng, Y. Liu, X. Hu and X. Zhang, *Green Chem.*, 2021, **23**, 1466–1494.
5 H. Cheng, J. Cheng, L. Wang and H. Xu, *Chem. Mater.*, 2022, **34**, 4259–4273.
6 X. Wang, Z.-Y. Yi, Y.-Q. Wang and D. Wang, *Angew. Chem., Int. Ed.*, 2025, **64**, e202413673.
7 J.-Y. Yue, J.-X. Luo, Z.-X. Pan, Q. Xu, P. Yang and B. Tang, *Angew. Chem., Int. Ed.*, 2025, **64**, e202417115.
8 J.-Y. Yue, L.-P. Song, Z.-X. Pan, P. Yang, Y. Ma, Q. Xu and B. Tang, *ACS Catal.*, 2024, **14**, 4728–4737.
9 Y. Liu, L. Li, Z. Sang, H. Tan, N. Ye, C. Sun, Z. Sun, M. Luo and S. Guo, *Nat. Synth.*, 2025, **4**, 134–141.
10 Z. Luo, Y. Yan, R. Spinney, D. D. Dionysiou, F. A. Villamena, R. Xiao and D. Vione, *Water Res.*, 2024, **261**, 122023.
11 H. Cheng, H. Lv, J. Cheng, L. Wang, X. Wu and H. Xu, *Adv. Mater.*, 2022, **34**, 2107480.
12 C. Krishnaraj, H. Sekhar Jena, L. Bourda, A. Laemont, P. Pachfule, J. Roeser, C. V. Chandran, S. Borgmans, S. M. J. Rogge, K. Leus, C. V. Stevens, J. A. Martens, V. Van Speybroeck, E. Breynaert, A. Thomas and P. Van Der Voort, *J. Am. Chem. Soc.*, 2020, **142**, 20107–20116.
13 J. Yang, X. Zeng, M. Tebyetekerwa, Z. Wang, C. Bie, X. Sun, I. Marriam and X. Zhang, *Adv. Energy Mater.*, 2024, **14**, 2400740.
14 J.-Y. Yue, L.-P. Song, Z.-X. Pan, M. Cheng, X. Wang, Q. Xu and P. Yang, *Chem. Eng. J.*, 2025, **504**, 158983.
15 E. Zhou, F. Wang, X. Zhang, Y. Hui and Y. Wang, *Angew. Chem., Int. Ed.*, 2024, **63**, e202400999.
16 Y. Zhang, J. Qiu, B. Zhu, G. Sun, B. Cheng and L. Wang, *Chin. J. Catal.*, 2024, **57**, 143–153.
17 H. Yu, X. Zhang, Q. Chen, P.-K. Zhou, F. Xu, H. Wang and X. Chen, *Chem. Res. Chin. Univ.*, 2024, DOI: **10.1007/s40242-024-4213-3**.
18 Y.-N. Gong, X. Guan and H.-L. Jiang, *Coord. Chem. Rev.*, 2023, **475**, 214889.
19 B. Mishra, A. Alam, A. Chakraborty, B. Kumbhakar, S. Ghosh, P. Pachfule and A. Thomas, *Adv. Mater.*, 2024, 2413118.
20 M. Zhang, M. Lu, M.-Y. Yang, J.-P. Liao, Y.-F. Liu, H.-J. Yan, J.-N. Chang, T.-Y. Yu, S.-L. Li and Y.-Q. Lan, *eScience*, 2023, **3**, 100116.
21 D. Tan, R. Zhuang, R. Chen, M. Ban, W. Feng, F. Xu, X. Chen and Q. Wang, *Adv. Funct. Mater.*, 2024, **34**, 2311655.
22 J. Hao, Y. Tang, J. Qu, Y. Cai, X. Yang and J. Hu, *Small*, 2024, **20**, 2404139.
23 R. Liu, Y. Chen, H. Yu, M. Položij, Y. Guo, T. C. Sum, T. Heine and D. Jiang, *Nat. Catal.*, 2024, **7**, 195–206.
24 Z. Gong, Y. Gao, J. Li, Z. Cai, N. Liu and J. Jiang, *Angew. Chem., Int. Ed.*, 2025, e202423205.
25 L. Zhang, C. Wang, Q. Jiang, P. Lyu and Y. Xu, *J. Am. Chem. Soc.*, 2024, **146**, 29943–29954.
26 W. Zhang, M. Sun, J. Cheng, X. Wu and H. Xu, *Adv. Mater.*, 2025, **37**, 2500913.
27 F. Zhang, X. Lv, H. Wang, J. Cai, H. Wang, S. Bi, R. Wei, C. Yang, G. Zheng and Q. Han, *Adv. Mater.*, 2025, **37**, 2502220.
28 Z. Yong and T. Ma, *Angew. Chem., Int. Ed.*, 2023, **62**, e202308980.

29 Q. Xue, H. Li, P. Jin, X. Zhou and F. Wang, *Angew. Chem., Int. Ed.*, 2025, e202423368.
30 J. Cheng, Y. Wu, W. Zhang, L. Wang, X. Wu and H. Xu, *Adv. Mater.*, 2025, **37**, 2410247.
31 J.-Y. Yue, Z.-X. Pan, R.-Z. Zhang, Q. Xu, P. Yang and B. Tang, *Adv. Funct. Mater.*, 2025, **35**, 2421514.
32 Z. Xie, X. Chen, W. Wang, X. Ke, X. Zhang, S. Wang, X. Wu, J. C. Yu and X. Wang, *Angew. Chem., Int. Ed.*, 2024, **63**, e202410179.
33 H. Xu, S. Xia, C. Li, Y. Li, W. Xing, Y. Jiang and X. Chen, *Angew. Chem., Int. Ed.*, 2024, **63**, e202405476.
34 H. Yu, F. Zhang, Q. Chen, P.-K. Zhou, W. Xing, S. Wang, G. Zhang, Y. Jiang and X. Chen, *Angew. Chem., Int. Ed.*, 2024, **63**, e202402297.
35 Y. Luo, B. Zhang, C. Liu, D. Xia, X. Ou, Y. Cai, Y. Zhou, J. Jiang and B. Han, *Angew. Chem., Int. Ed.*, 2023, **62**, e202305355.
36 W. Wu, Z. Li, S. Liu, D. Zhang, B. Cai, Y. Liang, M. Wu, Y. Liao and X. Zhao, *Angew. Chem., Int. Ed.*, 2024, **63**, e202404563.
37 D. Chen, W. Chen, Y. Wu, L. Wang, X. Wu, H. Xu and L. Chen, *Angew. Chem., Int. Ed.*, 2023, **62**, e202217479.
38 X. Yan, B. Wang, J. Ren, X. Long and D. Yang, *Angew. Chem., Int. Ed.*, 2022, **61**, e202209583.
39 H.-H. Sun, Z.-B. Zhou, Y. Fu, Q.-Y. Qi, Z.-X. Wang, S. Xu and X. Zhao, *Angew. Chem., Int. Ed.*, 2024, **63**, e202409250.
40 C. Wu, Z. Teng, C. Yang, F. Chen, H. B. Yang, L. Wang, H. Xu, B. Liu, G. Zheng and Q. Han, *Adv. Mater.*, 2022, **34**, 2110266.
41 Q. Niu, W. Deng, Y. Chen, Q. Lin, L. Li, Z. Liu, J. Bi and Y. Yu, *ACS Energy Lett.*, 2024, **9**, 5830–5835.
42 M. Bonchio, J. Bonin, O. Ishitani, T.-B. Lu, T. Morikawa, A. J. Morris, E. Reisner, D. Sarkar, F. M. Toma and M. Robert, *Nat. Catal.*, 2023, **6**, 657–665.
43 L. Guan, Z. Li, K. Wang, L. Gong, Y. Fang, G. Yu, M. Zhu and S. Jin, *Angew. Chem., Int. Ed.*, 2025, **64**, e202419867.
44 H. Yan, Y. Peng, Y. Huang, M. Shen, X. Wei, W. Zou, Q. Tong, N. Zhou, J. Xu, Y. Zhang, Y.-X. Ye and G. Ouyang, *Adv. Mater.*, 2024, **36**, 2311535.
45 Y. Yang, Y. Dong, W. Chi, X. Sun, J. Su, X. Chen, H. Zhao and Y. Zhu, *Chem. Eng. J.*, 2025, **503**, 158646.
46 X. Liu, R. Huang, L. Peng, J. Yang, J. Yan, B. Zhai, Y. Luo, C. Zhang, S. Tan, X. Liu, L. Ding and Y. Fang, *Angew. Chem., Int. Ed.*, 2025, **64**, e202414472.
47 Q. Shen, Q. Song, Z. Mai, K.-R. Lee, T. Yoshioka, K. Guan, R. R. Gonzales and H. Matsuyama, *Sci. Adv.*, 2023, **9**, eadf6122.